Materials Advances

ROYAL SOCIETY OF CHEMISTRY

PAPER

View Article Online
View Journal | View Issue

Cite this: *Mater. Adv.*, 2026, 7, 1691

Niobium-oxide-based octahedral molecular sieves as novel anode materials for sodium-ion batteries

Y. Bhaskara Rao, Naser Tavajohi * and C. André Ohlin *

Sodium-ion batteries have emerged as the most promising alternative to lithium-ion batteries due to the advantages of high natural abundance, low cost, environmental friendliness, and retention of charge capacity at low temperatures. However, novel anode and cathode materials need to be developed. In this work, Sandia octahedral molecular sieves – a class of ion exchangers with the general formula, $Na_2Nb_{2-x}M^{IV}_xO_{6-x}(OH)_x{\cdot}H_2O$ (M = Ti, Zr; x = 0.04–0.40) – are introduced as novel anode materials for sodium-ion battery applications. In this study, sodium niobium titanium oxide, $Na_2Nb_{1.6}Ti_{0.4}O_{5.6}(OH)_{0.4}{\cdot}H_2O$ (Na-NTO), is prepared by a simple hydrothermal method, followed by exchange of the Na^+ ion in the SOMS structure by one of the eleven selected divalent or monovalent cations, after which the electrochemical properties of the ion-exchanged SOMS materials are investigated and compared with those of the unexchanged SOMS material. Exchanging sodium for divalent zinc delivered an enhanced specific capacity (196 mAh g^{-1} at 10 mA g^{-1} *vs.* 89 mAh g^{-1} for Na-NTO) at every current density, whereas exchange for cadmium delivered a high capacity retention of 72% at 50 mA g^{-1} after 100 cycles. The enhanced electrochemical performance is related to their lower ionic radii (compared to Na^+), higher selectivity, optimal pore size and higher Na^+-ion diffusion coefficient. While the performances of the materials investigated here are comparatively low, the present work provides an in-depth study of the effect of partial ion-replacement on electrochemical performance.

Received 8th September 2025,
Accepted 18th December 2025

DOI: 10.1039/d5ma01026h

rsc.li/materials-advances

1. Introduction

Lithium-ion batteries (LIBs), referred to as "rocking chair batteries", are extensively used in a variety of portable electronic devices and electric cars because of their extended lifespan, high energy density, low weight, and flexible design.[1] However, the material costs of LIBs keep rising as demand rises, due to the comparatively limited supply of lithium, which eventually may make it impossible to meet the demands for energy storage.[2,3] Sodium, the second lightest and smallest alkali metal after lithium, has similar chemical properties to lithium, while being more abundant and cheaper. As sodium-ion batteries (SIBs) exhibit a similar "rocking chair"-type electrochemical mechanism, they are of interest as alternatives for LIBs. Consequently, SIBs have been extensively investigated for stationary energy storage and low-speed electric vehicles, where their lower volumetric energy density is less critical.[4–6]

The anode is an important part of a battery, and in SIBs, the Na metal cannot be used as the anode material due to the high reactivity of metallic sodium with the organic electrolyte solvents, and dendrite formation during Na metal deposition.[3] It is thus crucial to identify a suitable anode material with a high reversible capacity, stable structure, and appropriate potential window for successful development of SIBs. Recently, intercalation-type M–Nb–O anode materials have been studied extensively due to their high cycling stability, safe operating potential and significant intercalation pseudocapacitive behavior.[7] Here, in this work we investigated novel anode materials which belong to a family of materials with the formula, $Na_2Nb_{2-x}Ti_xO_{6-x}(OH)_x{\cdot}H_2O$ (x = 0.4), for the first time for SIBs. A key feature of these materials is that they act as ion exchange materials, which allows for facile modification of the materials.

Nyman *et al.* introduced this new family of isostructural, variable composition class of ion exchange materials, also known as SOMS (Sandia octahedral molecular sieves), with the general formula, $Na_2Nb_{2-x}M^{IV}_xO_{6-x}(OH)_x{\cdot}H_2O$ (M = Ti, Zr; x = 0.04–0.40).[8] This new family is produced through the substitution of Ti or Zr in a nominal $NaNbO_3$ octahedral framework. The niobium (Nb) atom is at the heart of sodium niobate ($NaNbO_3$), a perovskite oxide in general, which is surrounded by six oxygen atoms in an octahedral configuration. Another key component of $NaNbO_3$ is that these $[NbO_6]$ units run throughout the crystal structure and provide the foundation for its distinct physical and chemical characteristics.[9] These SOMS materials could be useful in the fabrication of microelectronic devices and capturing of valuable materials

Department of Chemistry, Umeå University, Umeå 90187, Sweden.
E-mail: naser.tavajohi@umu.se, andre.ohlin@umu.se

such as chromium, cobalt and nickel from industrial effluents to reuse them. Obtaining a pure phase of SOMS materials is challenging.[8] The maximum Ti : Nb ratio for which it is possible to obtain a pure phase of SOMS is 1 : 4 (x = 0.4).[8] On the other hand, an increase in the ratio of Ti : Nb produces larger SOMS crystals with an amorphous titania-rich material as a byproduct, whereas a decrease in the ratio results in the formation of an orthorhombic perovskite phase as an impurity.[8] Tina *et al.* scaled up the synthesis of sodium niobium titanium oxide, $Na_2Nb_{1.6}M^{IV}_{0.4}O_{5.6}(OH)_{0.4}\cdot H_2O$ (Na-NTO), through a simple hydrothermal route and obtained a pure phase SOMS with a negligible amount of impurity,[10] thus this material was chosen in our study to investigate the electrochemical performance of the SOMS material as an anode in Na-ion batteries.

SOMS exhibit a typical ion-exchange behavior where the microscopic pores present in the structure can accommodate divalent cations, such as Ba^{2+}, Sr^{2+}, Co^{2+}, and Zn^{2+}, and trap them at negatively charged sites that have been vacated by ions with weaker charges.[11] The sodium in the structure exchanges selectively for divalent cations, and two of the three sodium sites are exchangeable. The framework composition, particularly the Nb : Ti ratio, influences the channel composition in such a way that the ion exchange takes place by the exchange of a sodium plus a proton for a divalent cation. For instance, a divalent Sr^{2+} in the solution exchanges for a proton and a sodium in the SOMS, and the charge balanced ion exchange takes place according to eqn (1).[8]

$$Na^{+}_{SOMS} + H^{+}_{SOMS} + Sr^{2+}_{solution} \rightarrow Sr^{2+}_{SOMS} + Na^{+}_{solution} + H^{+}_{solution} \quad (1)$$

In addition, it was known that the properties like ion exchange behavior and thermal stability are controlled by the proton population inside the channels, which is directly altered by changes in the Nb:Ti framework composition.[8] In our work, we loaded the Na-NTO material with mono- and divalent cations including Ba^{2+}, Sr^{2+}, Cd^{2+}, Zn^{2+}, Ni^{2+}, Co^{2+}, Mg^{2+}, Li^{+}, Ca^{2+}, K^{+} and Cs^{+} following which the materials were tested as anode materials for SIBs to evaluate the electrochemical performance, as well as they were compared with the unmodified Na-NTO SOMS material. Here, the monovalent and divalent cations were selected solely based on selectivity coefficients determined for a similar material in ref. 11 in order to investigate whether ions could be irreversibly incorporated in the SOMS framework, and whether this would affect the electrochemical performance of the SOMS material.

The basic Na-NTO material, $Na_2Nb_{1.6}Ti_{0.4}O_{5.6}(OH)_{0.4}\cdot H_2O$, was prepared through a simple and straightforward hydrothermal procedure based on the method reported by Nyman *et al.*,[8] but using hydrous niobium oxide (niobic acid, $Nb_2O_5\cdot nH_2O$), instead of commercially available crystalline niobium oxide or pentaethoxyl niobium (NbOEt), and sodium hydroxide. This method produced a pure SOMS phase at significantly shorter reaction times and lower temperatures compared to the published methods which require *ca.* 4 days of synthesis, followed by heat treatment at >200 °C.[12]

2. Experimental section

2.1. Material synthesis

The base material Na-NTO, $Na_2Nb_{1.6}Ti_{0.4}O_{5.6}(OH)_{0.4}\cdot H_2O$, was prepared by a hydrothermal reaction. In a typical process, 1.785 g of niobic acid ($Nb_2O_5\cdot nH_2O$; 40% H_2O w/w), 850 μL of tetra isopropyl titanium (TIPT; from TCI), 6.7 g of sodium hydroxide (VWR chemicals), and 5 mL of *tert*-butyl hydroperoxide (TCI) were mixed in 40 mL of DI water in a Teflon liner. Here, *tert*-butyl hydroperoxide was used to solubilize TIPT. After one hour of stirring, the Teflon liner containing the aqueous mixture was put inside an autogenically pressurised Parr reactor and heated for 12 h at 175 °C. After cooling, the precipitated product was washed with DI water thoroughly four times and dried at 60 °C to obtain the base material (Na-NTO). A typical reaction yielded approximately 2 g of the product.

Ion exchange was carried out by stirring for 6 h 10 ml of a 1 M aqueous solution of the appropriate amount of either $ZnCl_2$ (Sigma-Aldrich), or $CaCl_2$ (Sigma-Aldrich), or $BaCl_2\cdot 2H_2O$ (VWR chemicals), or $Co(NO_3)_2\cdot 6H_2O$ (Thermo Scientific), or KCl (Merck), or $MgCl_2$ (Sigma-Aldrich), or $Ni(ClO_4)_2$ (ROC/RIC chemicals), or $SrCl_2\cdot 6H_2O$ (Sigma-Aldrich), or LiCl (Sigma-Aldrich), or $CdCl_2\cdot 2.5H_2O$ (Fisher Scientific), or $CsCl_2$ (Sigma-Aldrich), to which 0.5 g of the Na-NTO base material was added as a solid. The solids were isolated on a frit and washed with DI water thoroughly and dried at 60 °C. The ion-exchange materials are named according to the replaced ion, *e.g.*, Na-NTO treated with the Zn^{2+} material is referred to as Zn-NTO *etc.*

2.2. Characterization of materials

X-ray diffraction (XRD) spectroscopy using Cu-Kα radiation on a PANalytical Xpert3 powder X-ray diffractometer was used to analyze the crystal structure of the materials. The samples were scanned at a step size of 0.02626° in the 2θ range of 5–60°. Profex software was used to conduct the Rietveld refinement. Thermogravimetric analysis (TGA) experiments were performed on a Mettler Toledo TGA/DSC 1 instrument with alumina as a standard and the samples (4–6 mg) were heated from 25 to 700 °C at a ramp rate of 10 °C min^{-1}. The whole measurement was carried out in 20 mL min^{-1} flow of N_2 gas. Scanning electron microscopy (SEM) images were obtained by using a Zeiss Merlin Schottky FE-SEM equipped with a GEMINI II column. The related image contains the acceleration voltage (also known as electron high tension, or EHT), prober current, and working distance. N_2 adsorption–desorption measurements were conducted by using a Micromeritics TriStar 3000 porosimeter. The isotherms were recorded at −196 °C after the samples were outgassed for two hours at 100 °C. The specific surface areas were collected using the Brunauer–Emmett–Teller (BET) method, and the pore volumes were calculated using the desorption isotherms. The pore size distributions were estimated using the Barret, Joyner, and Halenda (BJH) algorithm with the ASAP-2010 program. X-Ray photoelectron spectroscopy (XPS) was obtained using a Kratos Axis Ultra DLD electron spectrometer with a monochromated Al Kα source running at 150 W. Wide spectra were obtained using an analyzer pass energy of 160 eV, whilst individual

photoelectron lines were detected at 20 eV. Kratos software was used for spectral processing.

2.3. Electrochemical characterization

For the electrochemical tests, CR-2032 coin-type half cells with O_2 and H_2O levels < 0.5 ppm were fabricated in an argon-filled glove box (MBraun-MB10-compact). For each electrode, DI water was mixed with the active substance (80 wt%), Super P (Thermo Scientific) (15 wt%), and the sodium carboxymethylcellulose (CMC-MedChemExpress; 5 wt%) binder. The mixture was applied on a copper foil current collector (TMAXCN; 14 mm diameter and 0.1 mm thickness) and dried at 50 °C. The electrode loading was approximately 2–3 mg cm^{-2}. A glass microfiber filter (Whatman, Grade GF/F; 19 mm diameter) served as the separator, and the electrolyte was 1 M $NaClO_4$ (Thermo Scientific) in ethylene carbonate (EC, from AmBeed) and dimethyl carbonate (DMC, from TCI; 1 : 1 v/v). Coin cells were constructed using sodium metal as the counter/reference electrode. Cyclic voltammetry (CV) curves at different scan rates and electrochemical impedance spectra (EIS) in the frequency range of 10 mHz to 1 MHz were recorded using a Gamry 1010E interface workstation. A NEWARE CT-4008 battery tester was used to record the galvanostatic charge–discharge curves within a 0.01–2.5 V (*vs.* Na^+/Na) voltage window. All electrochemical measurements were performed at 20 °C.

2.4. *Ex situ* XRD and XPS

For *ex situ* XRD/XPS measurements, the cells were charged/discharged to selected voltages after three complete discharge–charge cycles and disassembled inside the argon-filled glove box with O_2 and H_2O levels < 0.5 ppm. Any residual electrolyte was washed with the DMC solvent after recovering the electrodes. Later, they were dried in the glove box for 24 h prior to characterization.

3. Results and discussion

Fig. 1 illustrates the preparation of the basic SOMS material, $Na_2Nb_{1.6}Ti_{0.4}O_{5.6}(OH)_{0.4}{\cdot}H_2O$ (Na-NTO), through a simple and straightforward hydrothermal synthesis, as well as the preparation of ion-exchanged SOMS materials (*e.g.* Zn-NTO).

Fig. 2a shows the crystal structure of the $Na_2Nb_2O_6{\cdot}H_2O$ or SOMS material which contains $[NaO_6]$ and $[Nb/TiO_6]$ octahedra, with the remaining Na^+ species occupying the channel sites within the crystalline framework.[12] The $[Nb/TiO_6]$ octahedra are connected like double chains parallel to the [010] direction, whereas the $[NaO_6]$ octahedra are connected in layers that are parallel to [001]. The assembly of these layers of the $[NaO_6]$ octahedra alternates with the layers of double chains of the $[Nb/TiO_6]$ octahedra along the length of the *c*-axis forming a 3D network of channels. Unlike the case with corner sharing, which is commonly seen in framework structures, both the $[Nb/TiO_6]$ and $[NaO_6]$ octahedra are asymmetrical due to edge-sharing. In addition, the $[NaO_6]$ octahedra are more flexible and distorted than the $[Nb/TiO_6]$ octahedra as the O–Na–O bond angles have larger deviations from 90 or 180° compared to that of O–Nb/Ti–O bond angles. Each of the extra Na (Na(3)) species is coordinated to four O atoms in a deformed, square-planar geometry, and is located along 1D channels that are

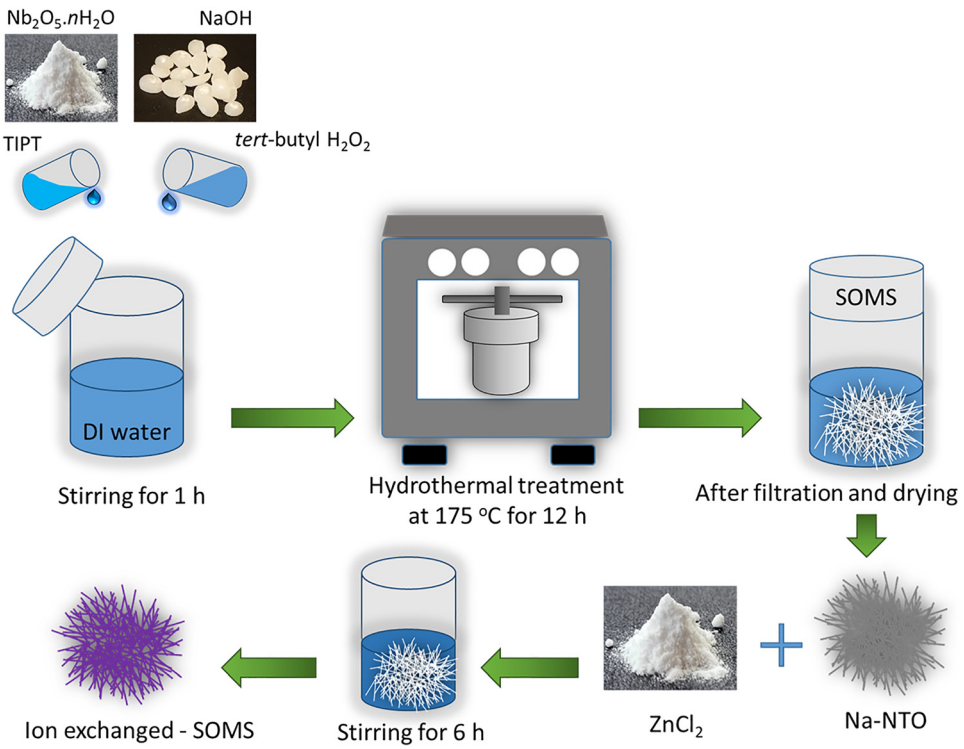

Fig. 1 Schematic illustration of the preparation of Na-NTO and ion-exchanged SOMS materials.

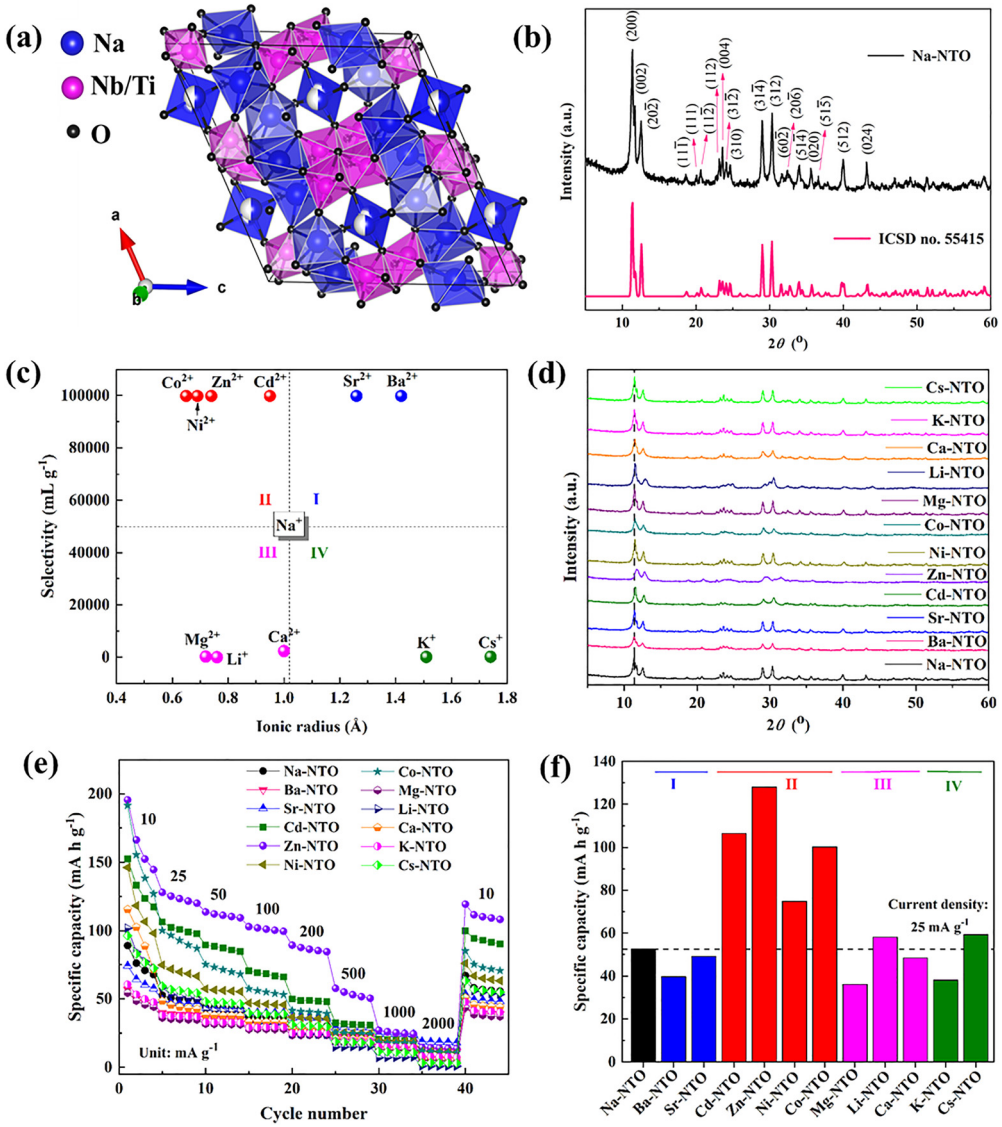

Fig. 2 (a) Structure of $Na_2Nb_2O_6{\cdot}H_2O$ (from ref. 12) and (b) XRD patterns of Na-NTO, (c) ion-exchange selectivity *vs.* ionic radius plot of selected divalent and monovalent ions, (d) XRD patterns of modified materials, (e) rate performance at various current densities, and (f) discharge specific capacity values (at a current density of 25 mA g^{-1}) of Na-NTO and the ion-exchanged SOMS materials Ba-NTO, Sr-NTO, Cd-NTO, Zn-NTO, Ni-NTO, Co-NTO, Mg-NTO, Li-NTO, Ca-NTO, K-NTO and Cs-NTO.

parallel to the *b*-axis. In particular, Na(3) is not located at the centre of a rectangle but rather at one of the two sites that are displaced from it.[12] Therefore, each Na(3) site has only 50% occupancy. Thus, this structure is unique in a manner that the extra cation also participates in forming the framework and creates distorted materials containing defect sites in the lattice.

Furthermore, the crystallinity and phase purity of the Na-NTO material were analyzed using XRD (Fig. 2b), which demonstrates that the product consists of pure phase Na-NTO with a monoclinic lattice assigned to the *C*2/*c* space group without any secondary phase impurities. All diffraction peaks, along with a high degree of crystallization, are perfectly matched with the major XRD reflections of the reported reference sample (ICSD no. 55415).[12] Different divalent (Ba^{2+}, Sr^{2+}, Ca^{2+}, Mg^{2+}, Co^{2+}, Ni^{2+}, Zn^{2+}, and Cd^{2+}) and monovalent (Cs^+, K^+, and Li^+) cations were selected.[11] Fig. 2c shows all the selected cations divided into four quadrants with respect to their ionic radii and selectivity (K_d from ref. 11) by assuming Na^+ (ionic radius – 1.02 Å) as the origin to better understand their properties. Quadrant I contains the ions with high selectivity and high ionic radius – Ba^{2+} and Sr^{2+} – whereas quadrant II contains the ions with high selectivity and low ionic radius, namely Cd^{2+}, Zn^{2+}, Ni^{2+}, and Co^{2+}. Quadrant III contains the ions with low selectivity and low ionic radius – Mg^{2+}, Li^+, and Ca^{2+} – while quadrant IV has the ions with low selectivity and high ionic radius – K^+ and Cs^+. After the Na^+-ion is exchanged with these cations, the ion-exchanged materials are obtained and exhibit the same phase and crystal structure as those of basic SOMS, the Na-NTO material which is confirmed by the XRD patterns shown in Fig. 2d.

Furthermore, the rate performance of all the ion-exchanged SOMS materials along with the basic SOMS material was evaluated at different current densities (Fig. 2e) and it is clear that at every current rate, the SOMS materials which are exchanged with the quadrant II elements, Cd-NTO, Zn-NTO, Ni-NTO and Co-NTO, showed better electrochemical performance compared to the other quadrant elements. For a better view, the reversible discharge specific capacities of all the materials at a current density of 25 mA g^{-1} are shown in Fig. 2f.

It is clear from the results that the ion-exchanged SOMS materials containing the ions from quadrants III and IV – Mg-NTO, Li-NTO, Ca-NTO and K-NTO, Cs-NTO, respectively – delivered poor discharge specific capacities, which was likely due to their low selectivity (Fig. 2c) causing them to revert back to Na-NTO in the presence of the sodium ion containing electrolyte of the coin cell battery. On the other hand, the divalent cations from quadrant I exhibit higher selectivity, yet the corresponding SOMS materials – Ba-NTO and Sr-NTO – showed lower discharge capacities compared to that of the base material, Na-NTO, which may be due to their higher ionic radii (Fig. 2c) compared to that of Na^+, although the mechanism is not clear. Thus, it is evident that the ion-exchanged SOMS materials for which the divalent/monovalent cations exhibit higher selectivity and lower ionic radii (quadrant II) delivered better rate performance compared to the other SOMS materials, including Na-NTO. The best performing (quadrant II) ion-exchanged SOMS materials, Cd-NTO, Zn-NTO, Ni-NTO and Co-NTO, underwent further studies and were compared with unmodified Na-NTO.

The observed and calculated XRD patterns of SOMS materials (for quadrant II), before and after ion exchange, are determined by using the Rietveld refinement (using Profex software) which are shown in Fig. 3. In addition, the lattice parameters are given in Table 1, and it is clear that the unit cell volume is decreased for ion-exchanged materials compared to the basic SOMS (Na-NTO) material. It may be due to the fact that the ionic radii of quadrant II cations are less than that of Na^+ (Fig. 2c). Thus, the replacement of Na^+ with the selected divalent/monovalent cations does not disturb the fundamental structure of the SOMS and the molecular sieve framework remains stable even after the ion-exchange. Furthermore, Fig. S1 shows the TGA spectra of Na-NTO, Cd-NTO, Zn-NTO, Ni-NTO and Co-NTO materials and two weight loss events are observed, upon heating, for all the five materials. The weight loss that occurred in the range of 150–250 °C corresponds to the loss of framework water and hydroxyls, which varies from 5 to 9 wt% for the ion-exchanged and the basic SOMS materials. Another weight loss event that occurred below 150 °C may be due to the loss of surface water;[8] however, there is no further weight loss until 700 °C. Thus, it is evident from the TGA analysis that the ion-exchange process does not affect the thermal stability of SOMS materials.

The morphologies and microstructures of Na-NTO and the ion-exchanged material Zn-NTO were analyzed by SEM, as shown in Fig. 4. A fine needle-shaped morphology is observed both in the Na-NTO (Fig. 4a) and Zn-NTO (Fig. 4b) materials, and these needles are typically a few micrometers long and a few nanometers wide.[13] It is evident that the morphology of the basic SOMS material has not been altered after Na^+ is exchanged with Zn^{2+}. Furthermore, the uniform distribution of zinc as well as the other elements, such as Na, Nb, Ti and O, in the Zn-NTO material are confirmed by the EDX elemental mapping images (Fig. 4d–h). Thus, the presence of Zn indicates that the Na^+ ions are successfully exchanged with Zn^{2+}. Similarly, Fig. S2 confirms the uniform distribution of Na, Nb, Ti and O in Na-NTO. The specific surface areas and pore size distributions of four ion-exchanged SOMS materials, Cd-NTO, Zn-NTO, Ni-NTO and Co-NTO along with Na-NTO, were determined by analysing the N_2 adsorption–desorption isotherms (Fig. 4i and j). The samples Cd-NTO, Zn-NTO, Ni-NTO and Co-NTO exhibited higher Brunauer–Emmett–Teller (BET) specific surface areas (S_{BET}) compared to the base material, Na-NTO (Table 2). With an increase in the specific surface area, the rate of sodium ion diffusion in the material and/or the kinetics of the sodium intercalation/deintercalation at the electrode/electrolyte interface can be greatly improved.[14] Furthermore, the Barrett–Joyner–Halenda (BJH) mean pore size of all the five materials was determined to be in the range of 12–18 nm (Table 2), suggesting that the SOMS materials are of mesoporous nature.[15]

Fig. 5a and b display the cyclic voltammetric curves of both Na-NTO and Zn-NTO electrodes for the three initial cycles, in the voltage range of 0.01–2.5 V. The cathodic and anodic peaks near 0.01 V observed in the CV curves in each case indicate the sodium insertion/extraction into/from the SOMS structure. The irreversible broad reduction peak at *ca.* 0.5 V in the first cycle is due to the formation of a solid electrolyte interphase (SEI) film and/or the electrolyte decomposition.[16] Similar behaviour is observed in other SOMS materials, Cd-NTO, Ni-NTO and Co-NTO, which are shown in Fig. S3a–c. However, sodium insertion and extraction are both highly reversible, which is evident from the overlapping CV curves in the subsequent cycles. Furthermore, the electrochemical performance of all five samples in the initial three charge–discharge cycles at a current density of 10 mA g^{-1} is shown in Fig. 5c, d and Fig. S3d–f. The unmodified SOMS material, Na-NTO, delivered the initial discharge and charge specific capacities of 218.44 and 60.60 mAh g^{-1}, respectively. On the other hand, the ion-exchanged SOMS materials, Cd-NTO, Zn-NTO, Ni-NTO and Co-NTO, delivered enhanced discharge/charge specific capacities of 376.27/133.91, 442.31/154.11, 504.51/104.36 and 487.10/138.03 mAh g^{-1}, respectively. For all the materials a high irreversible capacity loss was recorded in the first cycle and it may be due to the formation of an SEI layer, or the degradation of the liquid electrolyte, which is consistent with the CV results. Additionally, during the initial discharge cycle, some Na^+ ions may become irreversibly trapped in the pores of the (sponge-like) SOMS structure. However, the loss is greatly reduced from the second cycle and the reversible (second discharge) capacities of all the five materials are given in Table 2. Furthermore, it is observed that the coulombic efficiency is greatly improved (>75%) in all the five samples from the third charge–discharge cycle. Thus, the SOMS

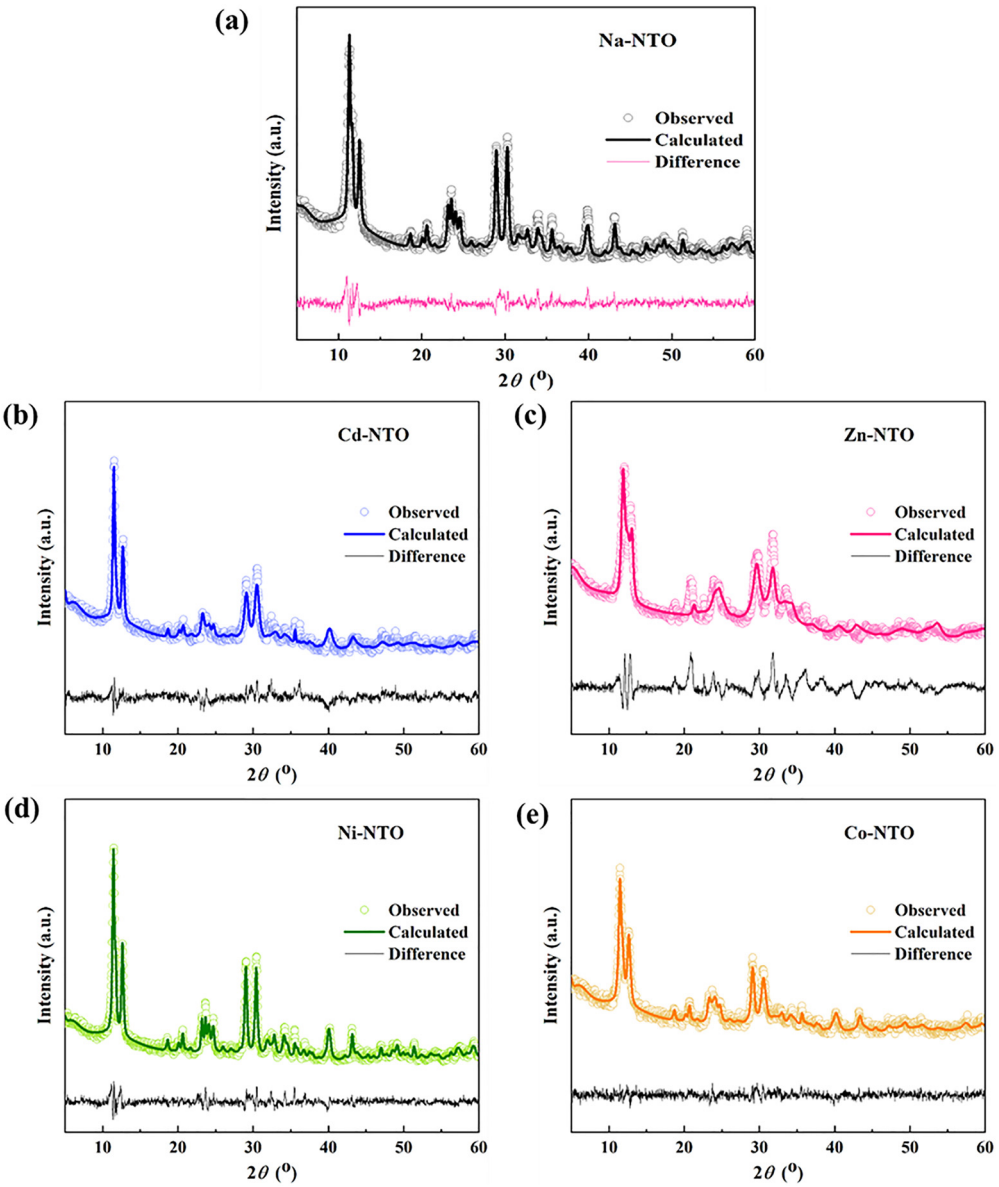

Fig. 3 Rietveld refined XRD patterns of (a) Na-NTO, (b) Cd-NTO, (c) Zn-NTO, (d) Ni-NTO and (e) Co-NTO materials.

Table 1 Structural details of Na-NTO, Zn-NTO, Cd-NTO, Ni-NTO and Co-NTO materials obtained from the Rietveld refinement

Sample name	Lattice parameters				Unit cell volume (Å^3)	Goodness of fit (GoF)
	a (Å)	b (Å)	c (Å)	β (°)		
Na-NTO	16.995(1)	5.032(7)	16.478(1)	113.96(4)	1287.74(9)	1.47
Zn-NTO	17.221(6)	4.979(0)	16.327(2)	115.08(1)	1267.94(1)	2.67
Cd-NTO	16.880(6)	5.048(5)	16.387(5)	114.11(6)	1274.52(7)	1.59
Ni-NTO	16.880(6)	5.046(1)	16.436(8)	114.01(4)	1278.82(8)	1.47
Co-NTO	16.880(6)	5.031(1)	16.366(9)	114.25(2)	1267.21(6)	1.22

materials exhibit stable reversible electrochemical kinetics against the Na metal.

In order to have a better understanding of the insertion/extraction behavior of Na^+ ions, the coin-type cells are disassembled as described in the Experimental section to perform *ex-situ* XRD measurements. At 2θ values of 43.3° and 50.4°, the typical Cu peaks are visible (Fig. S4a). Furthermore, at a current density of 50 mA g^{-1}, the changes in the crystal structure of SOMS electrodes are examined during the charge/discharge process at (i) a fully charged state (2.5 V), (ii) discharged to

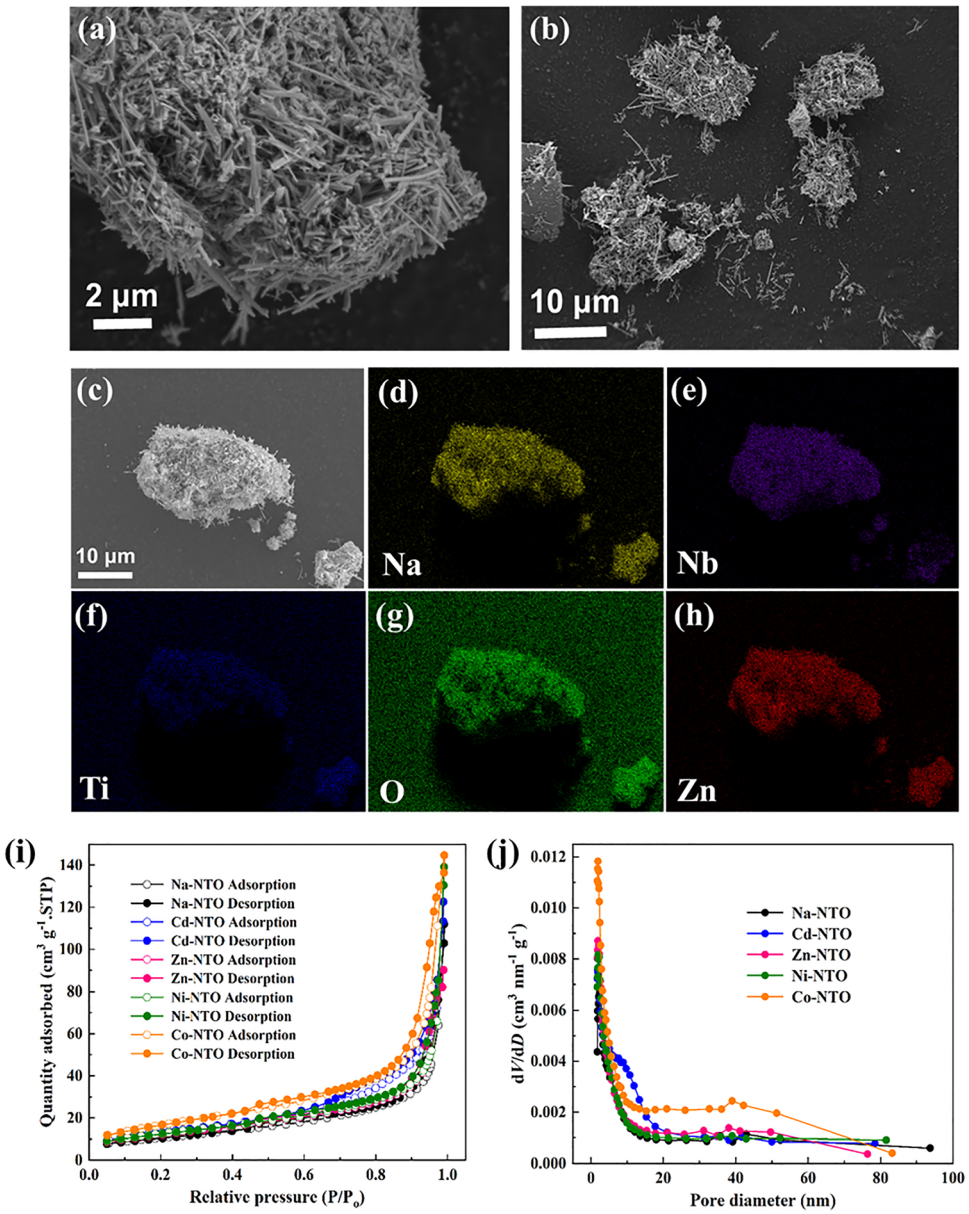

Fig. 4 SEM images of (a) Na-NTO and (b) Zn-NTO materials, (c)–(h) electron diffraction X-ray spectroscopy (EDX) images of the Zn-NTO material, (i) N_2-adsorption and desorption isotherms and (j) pore size distribution of Na-NTO, Cd-NTO, Zn-NTO, Ni-NTO and Co-NTO materials.

1 V and (iii) discharged to 0.01 V *vs.* Na^+/Na. As shown in Fig. S4b, the high intensity diffraction peak (200) moves to a lower angle during the discharging process from 2.5 V to 0.01 V, signifying the expansion of the crystal structure along the *a*-direction.[17] Similar behaviour is seen in all other four electrodes (Fig. S4c–f).

Ex situ XPS was performed on a Cd-NTO electrode for further confirmation of the Na^+-ion insertion mechanism. The survey spectrum (Fig. 6a) of pristine Cd-NTO contains Na 1s, Cd 3d, Nb 3d, Ti 2p and O 1s peaks positioned at binding energies of *ca.* 1071, 405, 207, 458 and 530 eV, respectively. From Fig. 6b, it is clear that no shift has occurred for the Cd $3d_{5/2}$ (405.7 eV) and $3d_{3/2}$ (412.5 eV) peaks, probably due to its fixed position in the Cd-NTO structural framework, which indicates that Cd^{2+} remains electrochemically inactive during Na^+-ion insertion. However, a systematic core-level peak shift, toward lower binding energy, is observed in the case of Nb/Ti upon discharge.[18,19] A significant peak shift is observed for Nb $3d_{5/2}$ (207.4 eV) and Nb $3d_{3/2}$ (210.2 eV) toward a lower binding energy side (207 and 209.7 eV, respectively) during Na^+-ion insertion consistent with the reduction of Nb^{5+} to Nb^{4+} (Fig. 6c). A similar phenomenon is observed in the case of Ti 2p, as shown in Fig. 6d, where the peaks, $2p_{3/2}$ (458.9 to 458.7 eV) and $2p_{1/2}$ (464.7 to 464.4 eV), are shifted to lower binding energies, which may correspond to a partial reduction of Ti^{4+} to Ti^{3+}, upon sodium insertion. Thus, the *ex situ* XRD/XPS results reveal the electrochemical sodiation/desodiation process which is governed by Nb/Ti redox reactions.

Table 2 The BET specific surface area, pore size, discharge specific capacity at 10 mA g^{-1}, σ (slope of Z' *vs.* $\omega^{-1/2}$ plot) and Na-ion diffusion coefficient from EIS, and b values from the power law for the SOMS materials, Na-NTO, Cd-NTO, Zn-NTO, Ni-NTO and Co-NTO

Sample	S_{BET} (m^2 g^{-1})	Pore size (nm)	Specific capacity (mAh g^{-1})	σ	D_{Na^+} (cm^2 s^{-1})	b
Na-NTO	38.48	18.00	88.96	31.2	9.06×10^{-12}	0.86
Cd-NTO	48.07	15.77	152.49	10.4	8.16×10^{-11}	0.87
Zn-NTO	45.02	12.39	195.56	15.9	3.49×10^{-11}	0.90
Ni-NTO	45.79	18.79	146.31	19.6	2.29×10^{-11}	0.84
Co-NTO	61.76	14.49	191.48	18.5	2.57×10^{-11}	0.83

Fig. 7a shows the rate performance of five SOMS materials at different current densities starting from 10 to 2000 mA g^{-1}. The initial coulombic efficiencies of all the materials are determined to be quite poor, and they are 34.8, 35.5, 20.6, 28.3 and 27.7% for Zn-NTO, Cd-NTO, Ni-NTO, Co-NTO and Na-NTO materials, respectively; however, the coulombic efficiencies are significantly improved from the subsequent cycles. Furthermore, the unmodified SOMS material, Na-NTO, displayed the discharge specific capacities of 88, 52, 43, 36, 29, 20, 13 and 2 mAh g^{-1} at current densities of 10, 25, 50, 100, 200, 500, 1000 and 2000 mA g^{-1}, respectively. On the other hand, the ion-exchanged material Cd-NTO delivered the enhanced discharge specific capacities of 152, 106, 89, 70, 49, 32, 20 and 5 mAh g^{-1}, whereas Co-NTO delivered the discharge specific capacities of 191, 100, 75, 57, 41, 25, 18 and 11 mAh g^{-1}, respectively, at the same current densities. Also, the ion-exchanged material, Ni-NTO, delivered the discharge specific capacities of 146, 74, 57, 46, 36, 25, 19, and 11 mAh g^{-1}, respectively. However, the Zn-NTO material delivered the high discharge specific capacities of 195, 128, 113, 102, 89, 57, 26, and 14 mAh g^{-1}, respectively, at the same current densities among the other samples. Furthermore, it is important to note that in all five materials, when the current density is returned to the initial value (10 mA g^{-1}), the discharge specific capacities are almost returned to their initial values which demonstrates their high reversibility and significant stability. Thus, the high rate capability in all ion-exchanged SOMS materials is attributed to their high specific surface area (see Table 2) compared to the unmodified material (Na-NTO) as the large surface area is beneficial for more reaction sites and shorter diffusion paths for ionic transport and electronic conduction.[20] Furthermore, long-term cycling stability over 100 cycles of all the five materials is shown in Fig. 7b at a current density of 50 mA g^{-1} in the voltage range of 0.01 and 2.5 V. It is clear from the figure that all samples delivered consistent coulombic efficiencies of above 99% during the cycling. Here, the unmodified SOMS material, Na-NTO, delivered a discharge specific capacity of only 24 mAh g^{-1} after 100 cycles which corresponds to a capacity retention of 54%. It may be due to the increase in its interfacial resistance that resulted from the reaction between the electrode and the organic electrolyte.[21] Conversely, superior reversible capacities of 72, 74, 36 and 43 mAh g^{-1} were recorded for Cd-NTO, Zn-NTO, Ni-NTO and Co-NTO materials, respectively, after 100 cycles. Thus, the

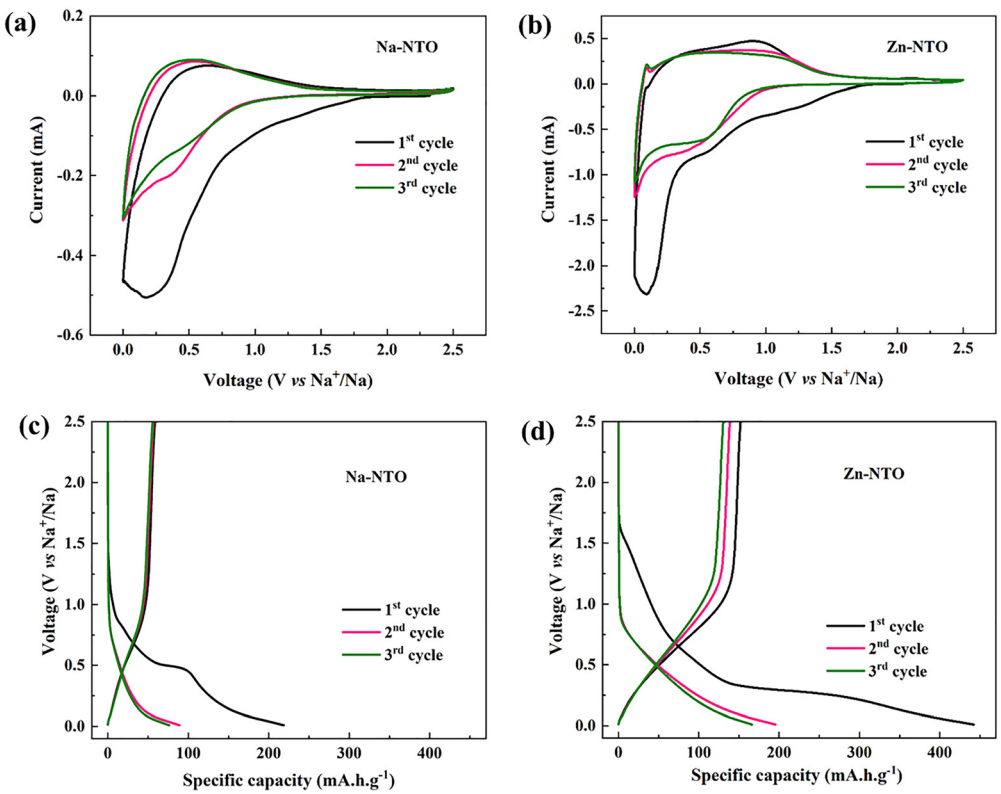

Fig. 5 Cyclic voltammetric and galvanostatic charge–discharge curves of Na-NTO (a) and (c) and Zn-NTO (b) and (d) materials for the first three cycles.

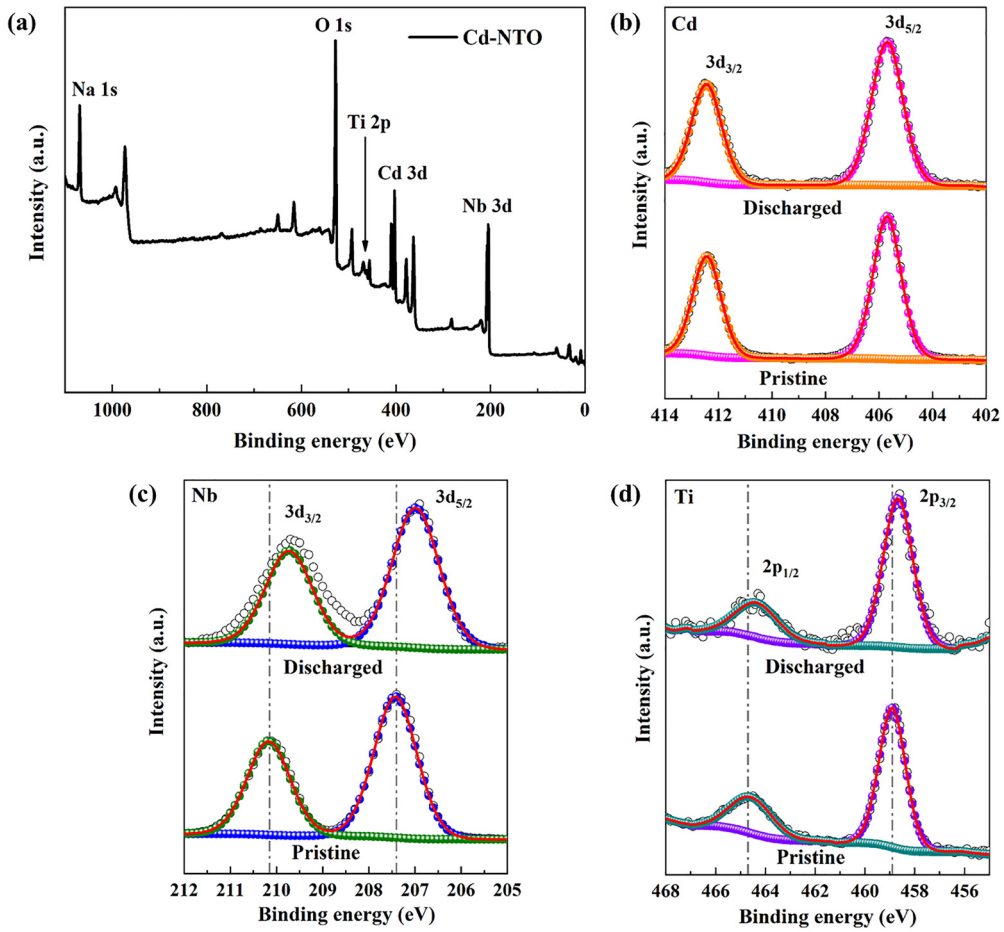

Fig. 6 (a) XPS survey spectrum of the pristine Cd-NTO sample, and *ex situ* XPS spectra of (b) Cd 3d, (c) Nb 3d and (d) Ti 2p of pristine and the discharged Cd-NTO electrode.

materials Zn-NTO, Ni-NTO and Co-NTO exhibited a significant capacity retention of 60%, while the material, Cd-NTO, delivered a high capacity retention of 72%. Furthermore, the electrochemical performance of ion-exchanged SOMS materials is compared with that of some other reported anode materials for SIBs in Table 3.

The enhanced rate and cycling performances were further analysed with the help of electrochemical impedance spectroscopy for the four ion-exchanged materials along with the unmodified SOMS material, before and after 10 cycles of discharge and charge (Fig. 7c, d and Fig. S5). The equivalent circuit, shown in the inset of Fig. 7c, is used to fit the Nyquist plots, where R_s represents the solution resistance, R_{SEI} is the SEI layer resistance, and R_{ct} is the charge transfer resistance.[22] A high SEI resistance of 56 Ω is observed in the case of Na-NTO, whereas negligible SEI resistance values, such as, 8, 7, 4 and 6 Ω, are found for the ion-exchanged SOMS materials, Cd-NTO, Ni-NTO, Co-NTO and Zn-NTO, respectively. In the case of the Na-NTO electrode, a higher charge transfer resistance of 69 Ω is recorded after cycling. On the other hand, significantly smaller charge transfer resistances of 22, 38 and 37 Ω are recorded for the ion-exchanged SOMS materials Cd-NTO, Ni-NTO and Co-NTO, respectively. Interestingly, for the Zn-NTO material a charge transfer resistance of 61 Ω was recorded, which is somewhat a higher value compared to those of other ion-exchanged SOMS materials. It could be the possible reason for a rapid decrease in the specific capacity of the Zn-NTO material during the long-term cycling.

Furthermore, the improved electrochemical rate performance and cycling stability are directly related to the Na^+-ion diffusion coefficient, D_{Na^+}, which can be calculated using eqn (2),[23]

$$D_{Na^+} = \frac{R^2T^2}{2A^2n^4F^4C_{Na}{}^2\sigma^2} \quad (2)$$

where R is the gas constant, T is the temperature, F is the Faraday constant, n represents the number of transferred electrons, A is the effective working area of the electrode, σ is the slope of Z' *vs.* $\omega^{-1/2}$ and C is the Na^+-ion concentration. Using eqn (3),[24]

$$Z' = R_s + R_{SEI} + R_{ct} + \sigma\omega^{-1/2} \quad (3)$$

the slope (σ) values can be determined by using the plot between Z′ and $\omega^{-1/2}$ (Fig. 7e), and are given in Table 2. After substituting all the values in eqn (2), the Cd-NTO electrode exhibited a significantly higher sodium ion diffusion coefficient (Table 2), while the unmodified SOMS material, Na-NTO, exhibited a lower Na^+-ion diffusion coefficient compared to those of the other SOMS materials. Thus, the fast movement of

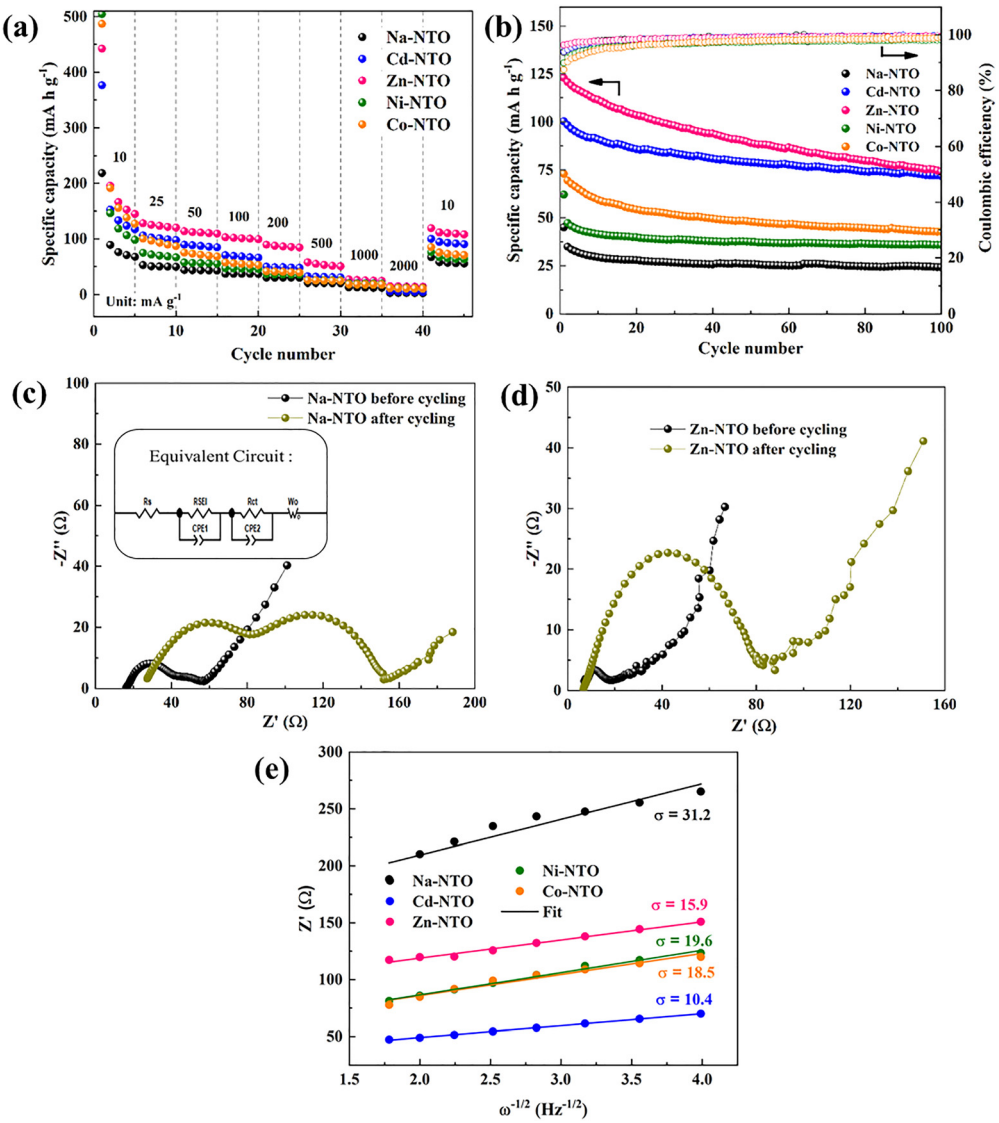

Fig. 7 (a) Rate performance at various current densities, and (b) cycling stability at a current density of 50 mA g^{-1} of Na-NTO, Cd-NTO, Zn-NTO, Ni-NTO and Co-NTO materials. Nyquist plots, before and after cycling of (c) Na-NTO (inset: equivalent circuit) and (d) Zn-NTO materials, and (e) fitting curves of Z' and $\omega^{-1/2}$ at a low frequency region of Na-NTO, Cd-NTO, Zn-NTO, Ni-NTO and Co-NTO materials.

Table 3 Comparison of electrochemical performance of ion-exchanged SOMS materials with that of some other reported anode materials for SIBs

Anode material	Preparation	Potential window (V *vs.* Na^+/Na)	Specific capacity (mAh g^{-1})	Current density	Ref.
Nb–TiO_2	Sol–gel	0.0–2.5	177.9	0.1C	25
$TiNb_2O_7$	Ball milling	0.01–2.5	180	15 mA g^{-1}	26
2-Nb_2C/BTC	Dehydration condensation reaction	0.0–3.0	164	100 mA g^{-1}	27
KNb_3O_8@F-C	Solution-assisted solid-state reaction	0.01–2.5	173	10 mA g^{-1}	28
$Zn_3Nb_2O_8$	Solvothermal	0.01–3.0	212.2	50 mA g^{-1}	29
Co-NTO	Hydrothermal	0.01–2.5	191.48	10 mA g^{-1}	This work
Zn-NTO	Hydrothermal	0.01–2.5	195.56	10 mA g^{-1}	This work

Na^+ ions, during the charge–discharge cycles, contributed to the enhanced electrochemical performance in the ion-exchanged SOMS materials.

The CV plots of Na-NTO, Cd-NTO, Zn-NTO, Ni-NTO and Co-NTO materials at different scan rates are displayed in Fig. 8 and Fig. S6. It is clear that the anodic and cathodic peak currents increase as the scan rate increases for all the materials. In addition, the redox peaks are more symmetric, which indicates that the electrodes exhibit a high reversibility. In all the materials, the oxidation peak shifted towards a higher potential

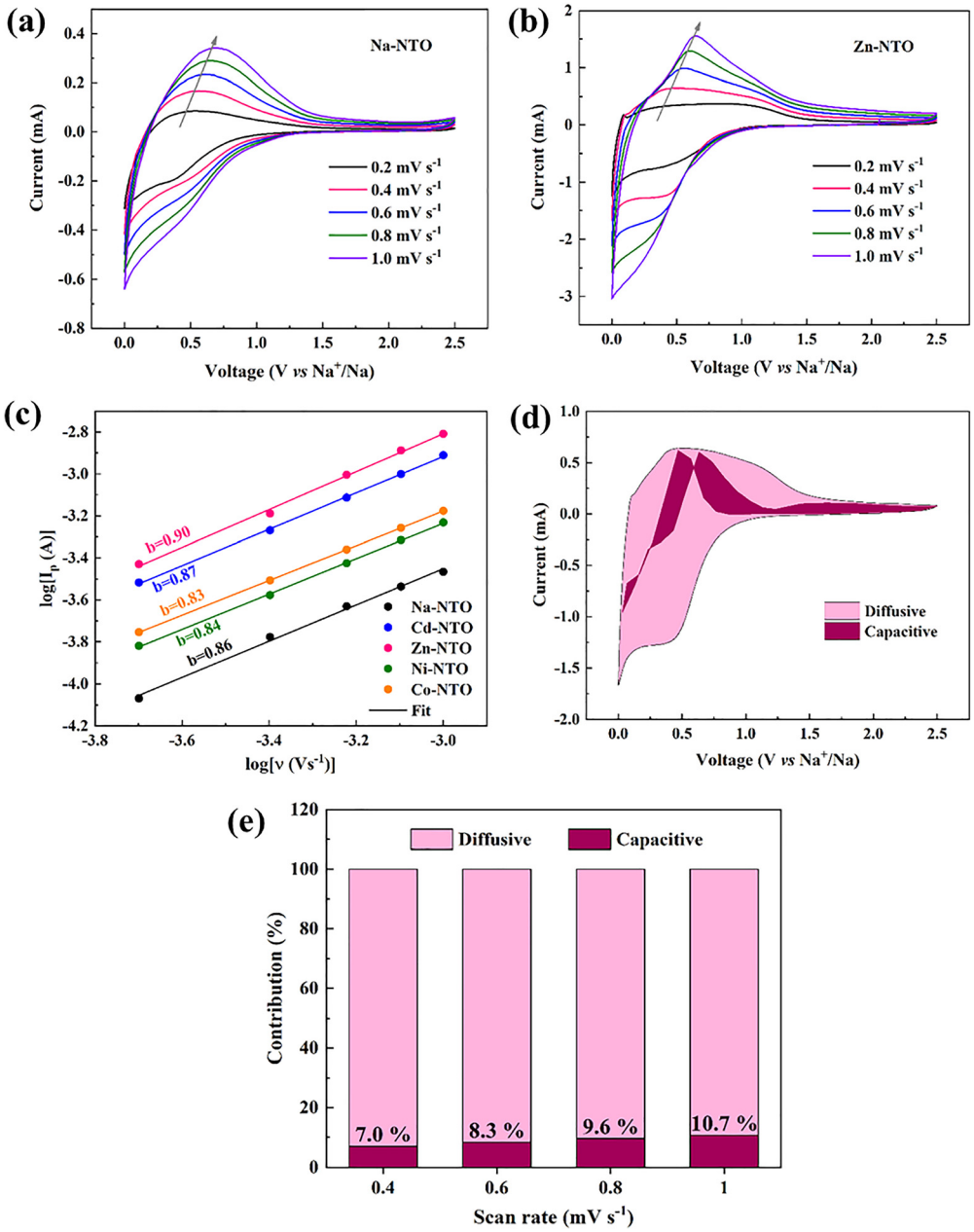

Fig. 8 Cyclic voltammograms at various scan rates of (a) Na-NTO and (b) Zn-NTO materials. (c) Plot of logarithm of scan rate *vs* logarithm of peak current of Na-NTO, Cd-NTO, Zn-NTO, Ni-NTO and Co-NTO materials, (d) CV curve showing the diffusive and capacitive contributions at a 0.4 mV s^{-1} scan rate, and (e) percentage contribution of diffusive and capacitive processes at various scan rates of the Zn-NTO material.

as the scan rate increases, indicating smaller polarization of the electrode materials.[30]

Furthermore, the power law relationship (eqn (4)) is used to investigate the electrode kinetics in the five SOMS materials,[31]

$$i_p = av^b \quad (4)$$

where i_p is the peak current, v is the scan rate, and a and b are constants determined from the fitting. Eqn (4) can be rewritten as eqn (5),

$$\log(i_p) = \log(a) + b\log(v) \quad (5)$$

Here, the slope b can be obtained from a linear fit of the graph between $\log(v)$ and $\log(i_p)$ (Fig. 8c), and the value can be used to determine the capacitive and diffusion-controlled contributions for the total capacity. From Table 2, the b value of all the five materials lies between 0.8 and 0.9, which indicates that the Na^+-ion storage mechanism is controlled by both capacitive and diffusive processes. Furthermore, the quantitative repartition of the diffusive and capacitive contributions to the overall storage mechanism of the Zn-NTO material is analysed using eqn (6),[28]

$$i(V) = k_1\nu + k_2\nu^{1/2} \quad (6)$$

where $k_1\nu$ and $k_2\nu^{1/2}$ represent the surface capacitive and the diffusion-controlled contributions, respectively. The capacitive and diffusive contributions on the CV plots of the Zn-NTO electrode at a scan rate of 0.4 mV s^{-1} are shown in Fig. 8d. It is clear from Fig. 8e that the percentage of capacitive contribution increases gradually as the scan rate increases from 0.4 to 1 mV s^{-1}. This may be due to the surface capacitance dominating the total capacity under high rate conditions. Consequently, the slow intercalation speed is unable to satisfy the needs of the high rate electrochemical processes at higher scan rates, which results in a decrease in the diffusion regulated capacity contribution.[32] Thus, the ion-exchanged SOMS materials, Cd-NTO, Zn-NTO, Ni-NTO and Co-NTO, exhibited significantly improved electrochemical performance due to the high selectivity and low ionic radii (SOMS associated with the cations from the quadrant II) compared to those of the other SOMS materials.

4. Conclusion

In summary, the isostructural ion-exchange SOMS material, Na-NTO, was prepared here by a facile one-step hydrothermal reaction using niobic acid as a precursor rather than the more complex and lengthy synthesis procedures which are available in the literature. Furthermore, on exchanging the Na^+ ions for other monovalent or divalent cations the electrochemical performance of the electrode materials in SIBs was changed. The SOMS materials, which are associated with the divalent cations selected from the quadrant II, Cd-NTO, Zn-NTO, Ni-NTO and Co-NTO, delivered higher discharge specific capacities compared to all other SOMS materials. In particular, the ion-exchanged material, Zn-NTO, exhibited a high specific capacity at every current density due to its optimal pore size and ionic radii, while the Cd-NTO material delivered a high capacity retention of 72% due to its high Na^+ ion diffusion coefficient and low charge transfer resistance. We believe that the detailed investigation and comparison of these ion-exchanged SOMS materials provide new insights on the development of novel anode materials for the Na-ion battery technology.

Author contributions

Y Bhaskara Rao: investigation, methodology, conceptualization, formal analysis, data curation, and writing – original draft. Naser Tavajohi: validation, supervision, resources, and visualization. C. André Ohlin: validation, supervision, resources, visualization, funding acquisition, writing – review and editing, and project administration.

Conflicts of interest

The authors declare no competing financial interest.

Data availability

Any data that support the findings of this study are included within the article and also included as a part of the supplementary information (SI). Supplementary information, including TGA, EDX and electrochemical data, is available. See DOI: https://doi.org/10.1039/d5ma01026h.

Acknowledgements

The authors thank the Kempe foundation (JCSMK22-0094) for financial support and acknowledge the facilities and technical assistance of the Umeå Centre for Electron Microscopy (UCEM) at the Chemical Biological Centre (KBC), Umeå University, SWEDEN.

References

1 Z. He, Y. Huang, H. Liu, Z. Geng, Y. Li, S. Li, W. Deng, G. Zou, H. Hou and X. Ji, *Nano Energy*, 2024, **129**, 109996.
2 S. W. Kim, D. H. Seo, X. Ma, G. Ceder and K. Kang, *Adv. Energy Mater.*, 2012, **2**, 710–721.
3 M. D. Slater, D. Kim, E. Lee and C. S. Johnson, *Adv. Funct. Mater.*, 2013, **23**, 947–958.
4 N. Yabuuchi, K. Kubota, M. Dahbi and S. Komaba, *Chem. Rev.*, 2014, **114**, 11636–11682.
5 Y. Li, Y. Lu, C. Zhao, Y. S. Hu, M. M. Titirici, H. Li, X. Huang and L. Chen, *Energy Storage Mater.*, 2017, **7**, 130–151.
6 A. Rudola, R. Sayers, C. J. Wright and J. Barker, *Nat. Energy*, 2023, **8**, 215–218.
7 Z. Du, Q. Liu, M. Cheng, J. Hu, T. Wei, W. Li, Y. Ling, X. Hu and B. Liu, *J. Mater. Sci.*, 2022, **57**, 5987–5997.
8 M. Nyman, A. Tripathi, J. B. Parise, R. S. Maxwell and T. M. Nenoff, *J. Am. Chem. Soc.*, 2002, **124**, 1704–1713.
9 H. Xu, M. Nyman, T. M. Nenoff and A. Navrotsky, *Chem. Mater.*, 2004, **16**, 2034–2040.
10 T. M. Nenoff, J. D. Pless, E. Michaels and M. L. F. Phillips, *Chem. Mater.*, 2005, **17**, 950–952.
11 M. Nyman, A. Tripathi, J. B. Parise, R. S. Maxwell, W. T. A. Harrison and T. M. Nenoff, *J. Am. Chem. Soc.*, 2001, **123**, 1529–1530.
12 R. F. Ali, M. Gascoine, K. Starosta and B. D. Gates, *RSC Appl. Interfaces*, 2025, **2**, 381–389.
13 H. Zhu, Z. Zheng, X. Gao, Y. Huang, Z. Yan, J. Zou, H. Yin, Q. Zou, S. H. Kable, J. Zhao, Y. Xi, W. N. Martens and R. L. Frost, *J. Am. Chem. Soc.*, 2006, **128**, 2373–2384.
14 Y. Xia, M. Yoshio and H. Noguchi, *Electrochim. Acta*, 2006, **52**, 240–245.
15 W. Li, J. Liu and D. Zhao, *Nat. Rev. Mater.*, 2016, **1**, 16023.
16 X. Zhu, X. Jiang, X. Liu, L. Xiao and Y. Cao, *Green Energy Environ.*, 2017, **2**, 310–315.
17 H. Nakayama, M. Nose, S. Nakanishi and H. Iba, *J. Power Sources*, 2015, **287**, 158–163.
18 P. Hu, T. Zhu, C. Cai, B. Mai, C. Yang, J. Ma, L. Zhou, H. J. Fan and L. Mai, *Adv. Funct. Mater.*, 2022, **32**, 2208051.

19 M. Asif, Z. Ali, H. Qiu, M. Rashad and Y. Hou, *ACS Appl. Energy Mater.*, 2020, **3**, 3541–3552.
20 S. Li, Q. Xu, E. Uchaker, X. Cao and G. Cao, *CrystEngComm*, 2016, **18**, 2532–2540.
21 F. Zheng, Q. Deng, W. Zhong, X. Ou, Q. Pan, Y. Liu, X. Xiong, C. Yang, Y. Chen and M. Liu, *ACS Sustain. Chem. Eng.*, 2018, **6**, 16399–16411.
22 Y. Zhuang, W. Zhang, Y. Bao and M. Guan, *J. Alloys Compd.*, 2022, **898**, 162848.
23 Y. Bhaskara Rao, N. Tavajohi and C. Andre Ohlin, *Batteries Supercaps*, 2025, **8**, e202500134.
24 Y. Wei, S. Zhu, J. Bai, X. Ma, B. Zhao, X. Zhu, Z. Zi and J. Dai, *Int. J. Electrochem. Sci.*, 2020, **15**, 9081–9087.
25 F. Zhao, B. Wang, Y. Tang, H. Ge, Z. Huang and H. K. Liu, *J. Mater. Chem. A*, 2015, **3**, 22969–22974.
26 Y. Huang, X. Li, J. Luo, K. Wang, Q. Zhang, Y. Qiu, S. Sun, S. Liu, J. Han and Y. Huang, *ACS Appl. Mater. Interfaces*, 2017, **9**, 8696–8703.
27 M. Liu, D. Zhang, B. Liu, C. Tian, B. Zhao, Y. Wang, Y. Wang, Y. Hu, L. Kong, D. Luo and Z. Chen, *Nano Energy*, 2022, **103**, 107795.
28 Y. B. Rao and C. A. Ohlin, *Sustain. Energy Fuels*, 2025, **9**, 2217–2227.
29 X. Yin, S. Cheng, Y. Zhang and C. Liu, *RSC Adv.*, 2024, **14**, 25571–25578.
30 B. He, J. Cunha, Z. Hou, G. Li and H. Yin, *J. Colloid Interface Sci.*, 2023, **650**, 857–864.
31 Y. B. Rao and C. A. Ohlin, *RSC Adv.*, 2025, **15**, 34300–34309.
32 S. Li, J. Qiu, C. Lai, M. Ling, H. Zhao and S. Zhang, *Nano Energy*, 2015, **12**, 224–230.